Corrosion Science 210 (2023) 110826

Contents lists available at ScienceDirect

Corrosion Science

journal homepage: www.elsevier.com/locate/corsci

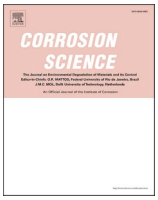

On the high-temperature oxidation of ZnSb for thermoelectric applications

Reshma K. Madathil [a], Vincent Thoréton [a], Øystein Prytz [b], Truls Norby [a,*]

[a] Department of Chemistry, Centre for Materials Science and Nanotechnology, University of Oslo, Gaustadalléen 21, NO-0349 Oslo, Norway
[b] Department of Physics, Centre for Materials Science and Nanotechnology, University of Oslo, P.O. Box 1048 Blindern, NO-0316 Oslo, Norway

ARTICLE INFO

Keywords:
ZnSb
Thermoelectric materials
Oxidation
XPS
TEM
Thermogravimetry
SIMS

ABSTRACT

Thermoelectric ZnSb has a native surface oxide layer of Sb_2O_5 +ZnO, while HT oxidation in air resulted in selective oxidation to ZnO, with no detectable Sb by STEM-EDS. The ZnO consisted of an inner nano-granular and a more columnar outer layer. Thermogravimetry showed parabolic oxidation kinetics at 200–325 °C with an activation energy of 117 kJ/mol, comparing well with literature for oxidation of Zn. Two-stage $^{16}O_2$ +$^{18}O_2$ oxidation followed by SIMS suggests growth by mixed Zn and O diffusion through a protective ZnO layer that still cannot prevent considerable high temperature oxidation in air, with formation of insulating electrical contacts, unless metallised.

1. Introduction

Thermoelectric (TE) materials convert heat in a temperature gradient into electrical energy [1,2]. Metallic TE materials exposed in air to the high temperatures that may be involved will degrade by oxidation. In particular, resistive oxide layers may form at their electrical contacts. Understanding and limiting the oxidation of metallic TE materials is therefore vital to the widespread use of thermoelectric generators (TEGs) at high temperatures.

ZnSb was early discovered and applied as a TE material [3], but while little improvement in efficiency reduced interest in the 1970 s, recent decades have brought a resurgence of interest in ZnSb as it provides a compromise between several important properties for TE materials. It is thermally stable, the average efficiency is competitive, and it is made up of abundant and non-toxic elements. However, studies of oxidation of ZnSb are scarce [4]. Berland et al. reported on oxygen contents of their prepared ZnSb samples [5]. Pothin reported that ZnSb alloy samples contained ZnO particles that affected mechanical properties [6]. In both cases, the oxygen was located at grain boundaries. Decomposition of ZnSb during heating in water vapour inside an E-TEM indicated that Zn sublimates and Sb remains near the surface [4]. In various other reports where ZnSb is synthesised, authors often specify that care was taken to avoid ZnSb oxidation. All in all, more knowledge is needed about oxidation of ZnSb and how it determines the degradation of ZnSb-based thermoelectrics, the device fabrication, and the design of new alloys.

In this work, the kinetics of oxidation of ZnSb at elevated temperatures in air was studied by thermogravimetry (TG) and the resulting oxide layer was investigated by X-ray photoelectron spectroscopy (XPS) and scanning transmission electron microscopy (STEM). Two-stage oxidation in $^{16}O_2$ and $^{18}O_2$ followed by secondary-ion mass spectroscopy (SIMS) depth profiling was performed to shed light on the dominating growth mechanism.

2. Materials and methods

2.1. Sample preparation

ZnSb was made by melting a 1:1 mixture of elemental Zn and Sb with purities of 99.99% in an evacuated quartz ampule that was subsequently quenched in water. The resulting ingot was crushed and ball milled using stainless steel balls and vial in Ar atmosphere before hot-pressing at 500 °C for 30 min at 20 MPa under N_2 flow in an in-house built hot-press. The hot-pressed disc was ground and polished with SiC paper to remove surface inhomogeneities and contaminants and cut into 5x5x5 mm^3 samples. The relative density of the hot-pressed samples was 98% as measured by the Archimedes method. X-ray diffraction of the powder before hot-pressing and of the hot-pressed sample both showed the ZnSb phase with additionally around 2–5 wt% metallic Sb. This amount of additional Sb phase is commonly seen in our samples and in other reported works [7]. For characterisation of oxide scales, samples were put in a tubular furnace and heat-treated at 325 °C in ambient air for 50, 115

* Corresponding author.
E-mail address: truls.norby@kjemi.uio.no (T. Norby).

https://doi.org/10.1016/j.corsci.2022.110826
Received 27 May 2022; Received in revised form 8 November 2022; Accepted 10 November 2022
Available online 13 November 2022

or 200 h.

2.2. Characterisation

XPS surface characterisation was done in a Kratos AXIS Ultra^{DLD} spectrometer with monochromatic Al Kα radiation ($h\nu$=1486.6 eV). The collected data were processed with the CasaXPS software package. The background was subtracted using a Shirley-Sherwood subtraction, and the spectra were energy calibrated to the carbon contamination C 1 s peak at 284.8 eV. Samples for scanning transmission electron microscopy (STEM) were made by focused Ga ion beam (FIB) milling in a JEOL 4500 Multibeam instrument. A protective carbon layer was deposited prior to the Ga milling in order to protect the sample from milling damage. Lamellae cut out with the FIB were studied in a JEOL 2100 F TEM at 200 kV with an Oxford X-Max 80 energy-dispersive X-ray spectrometer and with a FEI Titan G2 60–300 TEM at 300 kV with a FEI Super-X EDS detector, employing bright field (BF), annular dark field (ADF), and high angle annular dark field (HAADF) detectors for enhanced structural and atomic mass contrast. Data processing was done in the open-source python package Hyperspy [8] and Gatan Microscopy Suite Software package.

The ball-milled ZnSb powder was used for thermogravimetry in a Netzsch STA 449 thermobalance. Samples of estimated surface area 2.18 cm^2 were heated at a rate of 5 °C/min and kept at the target temperature under a flow of dry natural air 150–200 h.

The two-stage isotope exchange oxidation experiments were conducted in a horizontal tube furnace with an in-house gas phase analysis (GPA) system equipped with a quadrupole mass spectrometer (QMS) to monitor chemical and isotope compositions. The gases used were high purity oxygen (~99.99% ^{16}O) and labelled oxygen (fraction of $^{18}O \approx$ 97%). The specimens were placed in a quartz tube and after evacuation, the first isotope ($^{16}O_2$) was introduced. The quartz tube was then inserted into the furnace at 325 °C. At the end of the first stage of oxidation (after 12 h), the quartz tube was moved out of the hot zone for fast cooling, then evacuated at room temperature for 15 min for complete removal of the first oxidant isotope to ensure the same thermal conditions as first oxidation. Then we introduced the second oxidant $^{18}O_2$ and inserted the quartz tube back into the furnace still at 325 °C and kept it there for 24 h. At the end of the second stage, the samples were quenched by retraction out of the hot zone and subjected to SIMS profiling with a Cameca IMS 7 f Magnetic Sector SIMS. The primary beam (Cs^+, 15 kV) intensity was set to 10 nA and the raster size set to 200 μm. With a total sputtering time of 747 s, the crater depth was 432 nm as measured with a profilometer.

3. Results and discussion

3.1. X-ray photoelectron spectroscopy

XPS was done on a ZnSb sample kept at room temperature (RT) and a sample heated to 325 °C in ambient air for 115 h. Fig. 1a) and b) show spectra for the RT sample of the Sb 3d and O 1 s region and the Zn LMM Auger region, respectively. The two peaks in Fig. 1a) located at approximately 541 and 538 eV, originate from excitations of the Sb $3d_{3/2}$ orbitals and were fitted with a Gaussian-Lorentzian line shape. At lower energies, peaks are found from the $3d_{5/2}$ orbitals; these were fitted based on known values for peak shift and area relative to the 3/2 peaks. The signals were compared to reference values and identified as metallic Sb from ZnSb and an oxide of Sb, most likely Sb_2O_5. The remaining signal originates from O 1 s orbitals in various oxide compounds and were not assigned in more detail. For identification of Zn, the LMM Auger region was selected since the chemical shifts of the Zn 2p peaks are too small to identify different Zn species reliably. Fig. 1b) shows a similar observation for Zn as seen in Fig. 1a) for Sb, a metallic Zn signal from ZnSb and an oxide Zn signal from ZnO, indicating that a native mixed oxide layer forms at room temperature on ZnSb. Given the

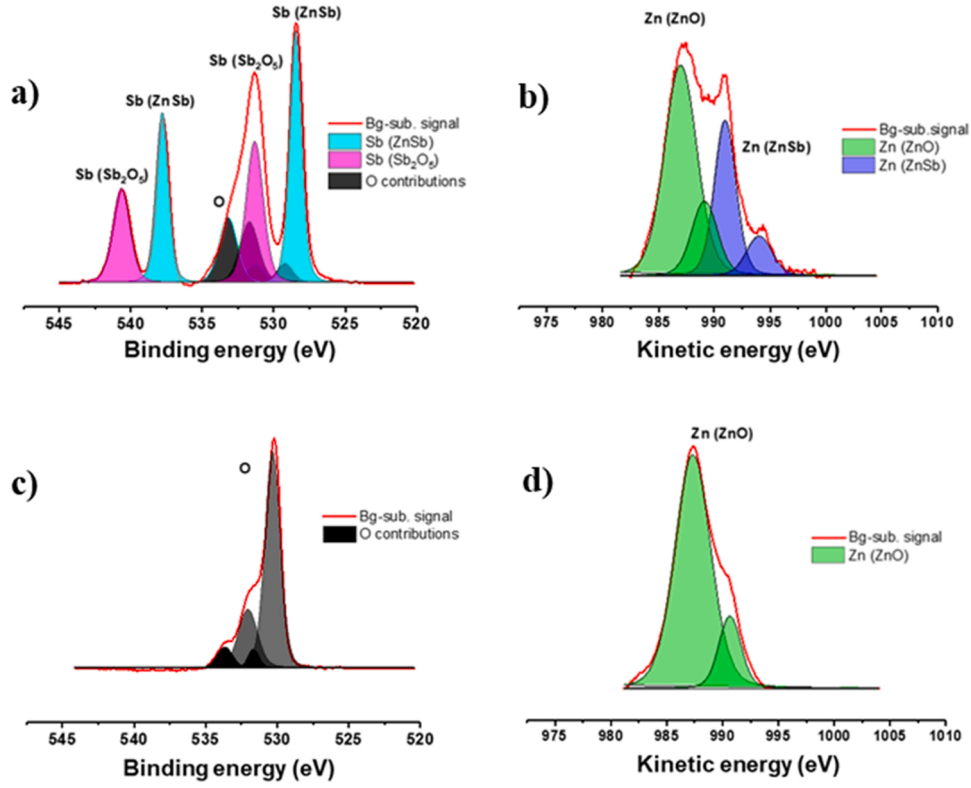

Fig. 1. XPS spectra collected from an unheated sample (a) and b)), and from a sample heated in air at 325 °C for 115 h (c) and d)). a) and c) show the Sb 3d and O 1s region where the heated sample (c)) no longer has any Sb 3d signal. b) and d) show the Zn auger LMM region where the heated sample (d)) only shows the presence of ZnO, no ZnSb as in the unheated sample (b)).

expected XPS signal depth, and the signal from ZnSb, the thickness of the native oxide layer is estimated to be only a few nanometres.

Fig. 1c) and d) show XPS spectra from the same energy ranges for a sample heated to 325 °C in air for 115 h. Significant changes are observed compared to the room-temperature spectra. The Sb 3d and O 1 s region in Fig. 1c) only shows various O 1 s signals and no Sb signal, and the Zn region in Fig. 1d) shows the presence of ZnO and no metallic Zn from ZnSb. Thus, heating ZnSb in air transformed the top surface of the sample from a thin layer of mixed oxide to a thick layer of pure ZnO.

3.2. STEM with EDS

FIB lamellae for STEM investigations were prepared of the oxidised ZnSb. A STEM-HAADF image of the oxide layer interface is shown in Fig. 2a) with an EDS line scan across the interface in Fig. 2c). The EDS line scan was taken from top to bottom in the image and showed a transition from mainly ZnSb 1:1 elemental composition with some O present to an oxide film consisting of ZnO. There is practically no Sb in the oxide layer. HAADF images are sensitive to variations in the average atomic number of the sample, hence the bright region is ZnSb, followed by a transition to the ZnO layer. The ZnO layer appears to have an interior lower intensity region and an outer higher intensity region. The EDS line scan shows no significant variation in elemental composition between these regions. Comparing the STEM-HAADF image with the more structurally sensitive STEM-ADF image of the same region (Fig. 2b)), the interior layer appears however to be finely grained, possibly amorphous, while the outer layer has columnar-type grains.

A STEM-HAADF image with EDS mapping of a heated sample is shown in Fig. 3, where it becomes clear that the Sb grains remain along the ZnSb-ZnO interface. As there is already a presence of metallic Sb grains in the pristine alloy, it is reasonable that additional Sb left behind from selective oxidation of Zn to ZnO, forming new grains of Sb or leads to growth of the existing ones. Sb remains completely unoxidised, and pure ZnO grows from selective oxidation of Zn.

Fig. 4 shows a STEM bright-field (BF) image with diffraction patterns from three different areas. Fig. 4b) shows the well-defined pattern of large (micrometre range) ZnSb grains. In the interfacial region, Fig. 4c), a ring pattern was observed indicating a more finely polycrystalline microstructure. If the region contained an amorphous phase as well, a large diffuse background intensity would have been visible. As this was not the case, we conclude that this region is composed of nanocrystalline ZnO grains. The outer region of the ZnO film has larger grains based on the diffraction, Fig. 4d), and were growing in a columnar fashion based on the STEM-ADF in Fig. 2b).

Neither we nor previous investigators of ZnSb oxidation find any Sb_2O_5 in oxide scale Zinc oxidation is favoured due to the more negative Gibbs free energy values of ZnO formation ($\Delta_f G^0 \sim -320$ KJ/mol) than that of Sb_2O_5 ($\Delta_f G^0 \sim -160$ KJ/mol).

3.3. Thermogravimetry

Weight gain curves of the crushed ZnSb samples in dry natural air are

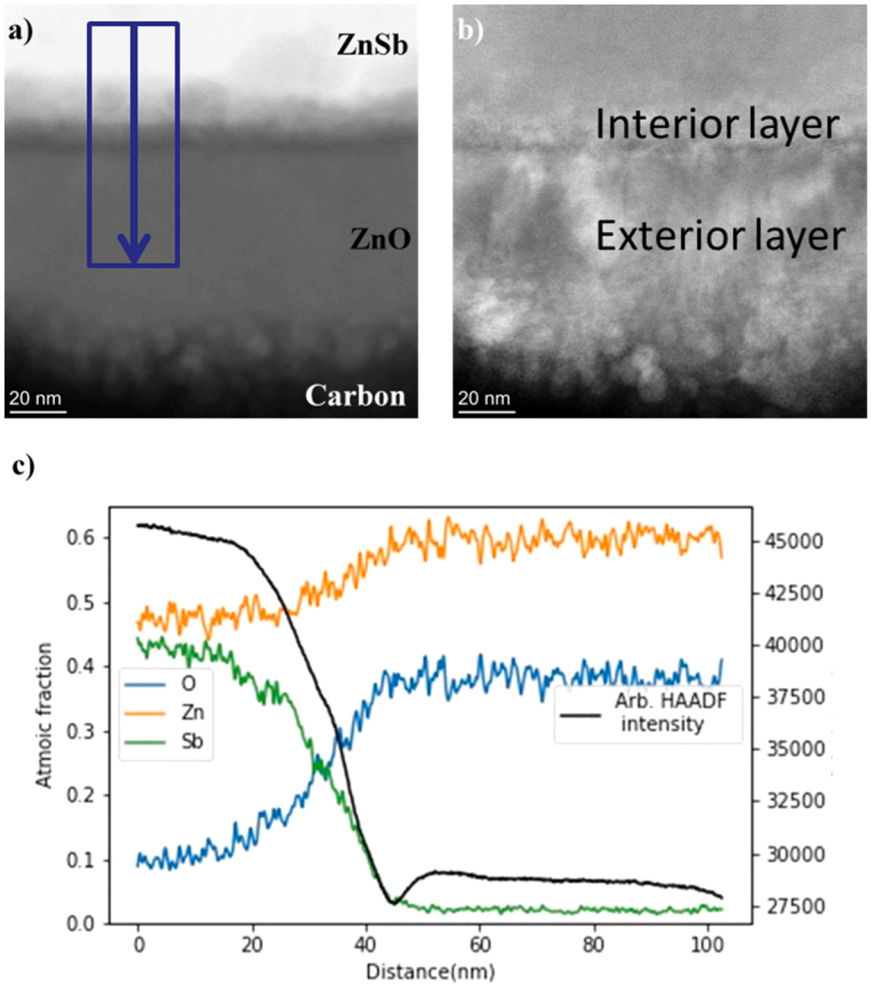

Fig. 2. Cross-section of oxide layer on ZnSb grown by heating in air for 115 h at 325 °C. a) STEM-HAADF image with EDS line scan range indicated. b) Corresponding STEM-ADF image showing that the ZnO scale has an interior nanograined and an exterior columnar layer. c) The EDS line scan across the interface between ZnSb and ZnO from the range indicated in a) shows that the oxide film in ZnO without any Sb. HAADF intensity is also plotted for easier alignment.

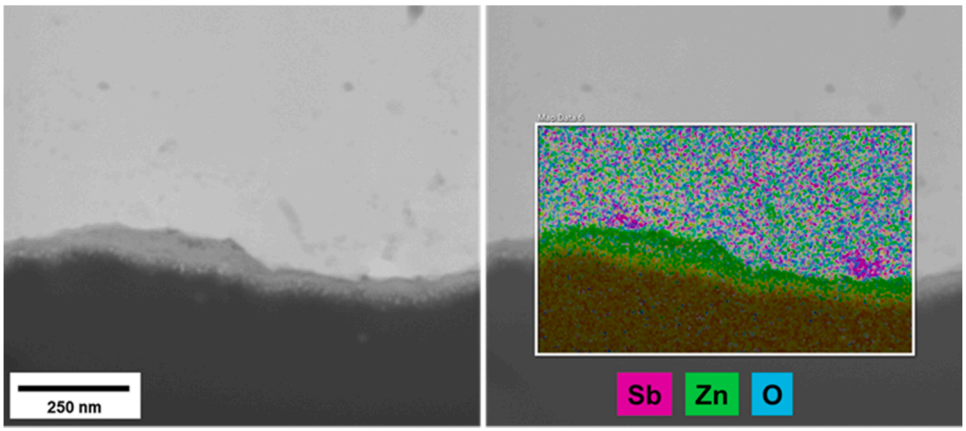

Fig. 3. STEM-HAADF image with EDS mapping of a heated sample reveals Sb-rich particles in the metallic phase along the interface to the oxide layer.

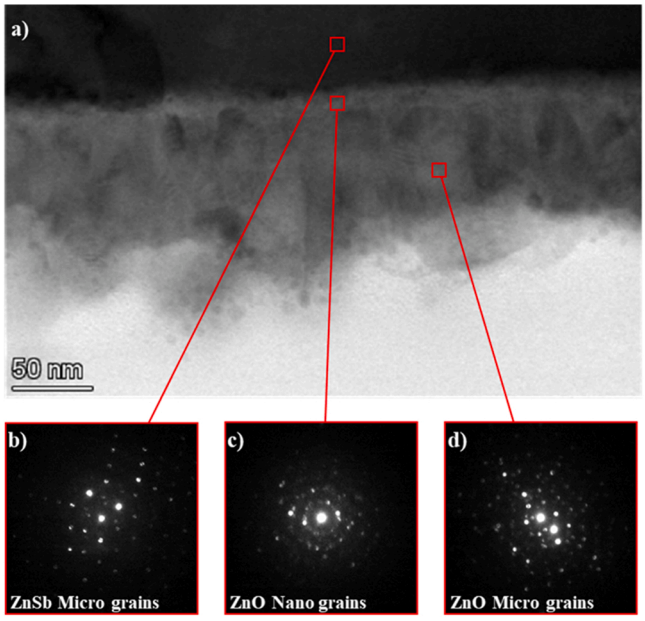

Fig. 4. ZnSb-ZnO interface as seen with STEM-BF in a). Microprobe diffraction images are shown in b), c) and d) taken from indicated areas in a).

shown in Fig. 5. There was no measurable mass gain below 150 °C. Essentially parabolic behaviour was first observed from 200 °C and upwards, while it at 325 ℃ showed beginning tendency of sub-parabolic kinetics.

The weight gain in each experiment for the range 200–325 °C was plotted as a function of the square root of time and fitted to the parabolic rate equation, allowing the calculation of the parabolic growth rate constant K_p, plotted in Fig. 6 as an Arrhenius plot of log K_p vs 1/T. The activation energy of 117 KJ/mol is in good agreement with reports of activation energies of 121 and 130 KJ/mol for oxidation of Zn foil [14] and Zn powder [15], respectively, substantiating that mainly ZnO forms during oxidation of ZnSb at elevated temperatures. Also, the K_p values in Fig. 6 are in good agreement with those for Zn oxidation obtained by

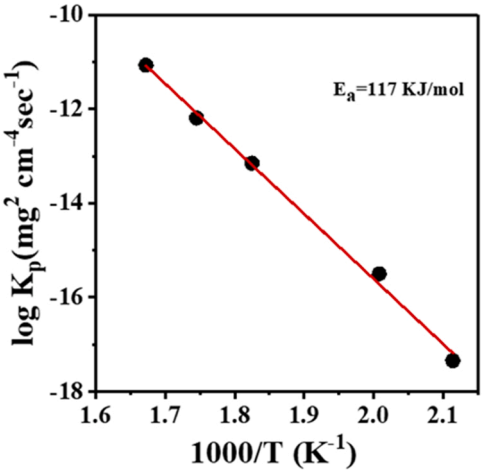

Fig. 6. Arrhenius plot of calculated parabolic oxidation rate constants from TG experiments, showing an activation energy E_a of 117 KJ/mol.

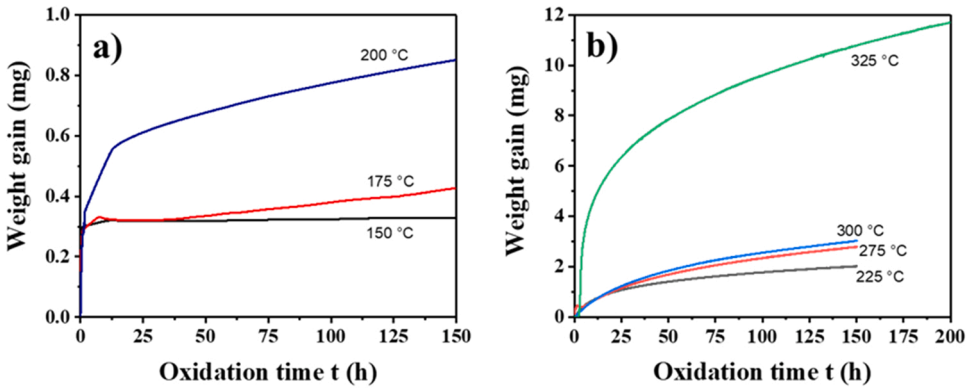

Fig. 5. a) Weight gain as a function of time for ZnSb powder of estimated surface area of 2.18 cm^2 in dry natural air at 150–200 °C (left) and 225–325 ℃ (right).

other workers at higher temperatures after extrapolation [14,16].

3.4. Two-stage oxidation

For the two-stage $^{16}O_2/^{18}O_2$ oxidation a sample of ZnSb was oxidised at 325 °C under 160 mbar of oxygen, first in $^{16}O_2$ for 12 h, then in $^{18}O_2$ for 24 h. A SIMS depth profile through the oxide layer is shown in Fig. 7, to a crater depth 432 nm. The second oxidant, ^{18}O, shows a clear signal at the surface of the oxide layer, but decays inwards, while the first oxidant, ^{16}O, increases inwards until the signal decays as the sputtered depth proceeds into the ZnSb substrate. Despite the longer annealing time in $^{18}O_2$ than in $^{16}O_2$, the outer part of the oxide because the oxide growth rate decreases with time. The profile with an accumulation of ^{18}O near the surface may indicate that the oxide grows outward, hence by diffusion of Zn through the oxide as the primary mechanism for oxidation [17,18], and agreement with the general view of faster diffusion of Zn by vacancies in bulk [11,12] and grain boundaries [13] than of O by interstitials [9,10] in ZnO under oxidising conditions. We note that the grain boundaries in the columnar outer layer provides a fast pathway for Zn diffusion in the growth direction [13]. However, the concentration of ^{18}O is still lower than that of ^{16}O even at the surface, so ^{18}O must be diffusing inwards also. All in all, it appears that both ions diffuse at not too different rates.

What is clear, however, is that there is no sign of short-circuit transport of gaseous O_2 through pores or cracks, as this would have given an ^{18}O peak close to the ZnO/ZnSb interface. While oxidation of pure Zn has a Pilling-Bedworth (P-B) ratio of volume of the oxide over that of the oxidising metal > 1, and forms a dense and protective oxide layer, selective oxidation of Zn in oxidation of ZnSb leaves a P-B ratio < 1 making the layer liable to crack. However, both the parabolic growth and the two-stage oxidation indicates that this is not the case, The nanocrystalline inner region of ZnO (Fig. 2) can thus not be a result of crack formation, but arise from early growth on top of or from transformation of the original mixed oxide layer.

3.5. Implications for ZnSb thermoelectrics

Many of the intermetallic TE materials with the highest figures of merit (ZT) suffer from high sublimation rates and poor oxidation resistance. The oxidation leads to decomposition and formation of a resistive oxide layer that limits functional stability and degrades electrical contacts. We have shown that oxidation of ZnSb forms a protective layer of ZnO, and the derived parabolic rate constants therefore allow estimates of the thickness of the ZnO oxide scale as a function of time at operation at a given temperature. If the growth is determined by diffusion of zinc vacancies, this may be difficult to suppress, since it would take acceptor doping, and it is notoriously difficult to effectively acceptor-dope ZnO. Instead, it is likely that substitutional or interstitial doping by Sb^{3+} or Sb^{5+} cations in addition to protons from ambient water vapour makes the ZnO layer inevitably donor doped, enhancing the concentration of zinc vacancies and hence diffusion and corrosion rate. For the electrical contacts, the donor doping of the ZnO layer may give it considerable n-type conductivity, but metallisation plating may still be needed for prolonged operation of ZnSb-based TE materials at elevated temperatures in air.

4. Conclusions

ZnSb oxidises in air at elevated temperatures by mainly parabolic growth of a dense, adherent, and protective layer of ZnO by selective oxidation of Zn, leaving remaining Sb in particles in the alloy near the interface. Outward diffusion of Zn dominates the growth mechanism, in agreement with literature data, although oxygen diffusion appears to be significant, too. The oxide grows in a columnar fashion, allowing enhanced diffusion of Zn along grain boundaries. A thin inner layer of nanocrystalline ZnO is speculated to arise in the initial stage of growth.

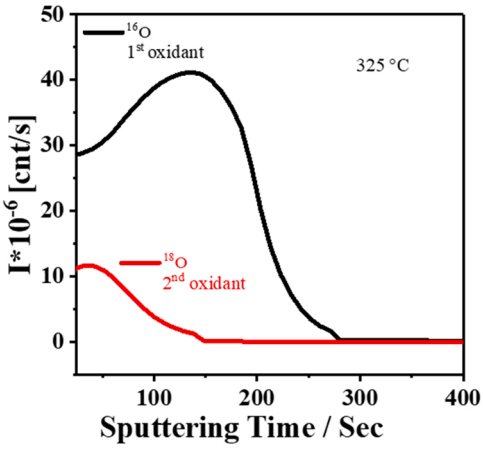

Fig. 7. SIMS profile of counts per second of oxidant isotopes in a two-stage oxidised ZnSb sample at 325 °C.

The empirical parabolic oxidation rate constant and its activation energy of 117 KJ/mol allow estimation of the thickness of the ZnO layer on ZnSb as a function of temperature and time of operation. It is likely that the oxide layer is effectively donor doped which increases the concentration of zinc vacancies as the main diffusing point defect, and that deliberate acceptor doping to counteract this is impossible. While the dominance of donors generally enhances the n-type conduction in the ZnO layer in electrical contacts, protective and/or metallisation plating appears generally important for prolonged use of ZnSb based TE intermetallics at elevated temperatures in air.

CRediT authorship contribution statement

Reshma K. Madathil: Conceptualization, Methodology, Investigation, Writing – original draft, Writing – review & editing, Visualization. **Vincent Thoréton:** Methodology, Investigation, Writing – review & editing. **Øystein Prytz:** Methodology, Resources, Writing – review & editing, Supervision. **Truls Norby:** Conceptualization, Resources, Writing – original draft, Writing – review & editing, Supervision.

Declaration of Competing Interest

The authors declare that they have no known competing financial interests or personal relationships that could have appeared to influence the work reported in this paper.

Data Availability

The authors are unable or have chosen not to specify which data has been used.

Acknowledgements

The Research Council of Norway is acknowledged for support to the Norwegian Centre for Transmission Electron Microscopy (NORTEM, 197405/F50), the National Surface and Interface Characterisation Laboratory (NICE, #195565), and the project “Fundamentals of Surface Kinetics in High Temperature Electrochemistry (FUSKE)” #262393). We are grateful to Prof. Reidar Haugsrud for advice and proofreading and to Dr. Christoph Seiffert for help with the SIMS measurements. As a PhD student at the Department of Physics, UiO, Henrik Riis contributed some of the experimental work reported here, but as he has become unreachable, we proceed to publish without him as co-author.

References

[1] G.S. Nolas, J. Sharp, J. Goldsmid. Thermoelectrics: Basic Principles and New Materials Developments, Springer Science & Business Media, 2001, pp. 1–13.
[2] G.D. Mahan, Introduction to thermoelectrics, APL Mater. 4 (10) (2016), 104806.
[3] X. Song, T. Finstad, Review of research on the thermoelectric material ZnSb. Thermoelectrics for Power Generation – A Look at Trends in the Technology, IntechOpen, 2016, pp. 117–145.
[4] X. Song, M. Schrade, N. Masó, T.G. Finstad, Zn vacancy formation, Zn evaporation and decomposition of ZnSb at elevated temperatures: influence on the microstructure and the electrical properties, J. Alloy. Compd. 710 (2017) 762–770.
[5] K. Berland, X. Song, P.A. Carvalho, C. Persson, T.G. Finstad, O.M. Løvvik, Enhancement of thermoelectric properties by energy filtering: theoretical potential and experimental reality in nanostructured ZnSb, J. Appl. Phys. 119 (12) (2016), 125103.
[6] R. Pothin, R.M. Ayral, A. Berche, D. Granier, F. Rouessac, P. Jund, Preparation and properties of ZnSb thermoelectric material through mechanical-alloying and spark plasma sintering, Chem. Eng. J. 299 (2016) 126–134.
[7] D.-B. Xiong, N.L. Okamoto, H. Inui, Enhanced thermoelectric figure of merit in p-type Ag-doped ZnSb nanostructured with Ag3Sb, Scr. Mater. 69 (5) (2013) 397–400.
[8] F. de la Peña, e.a., hyperspy/hyperspy: HyperSpy v1.5.2. 2019, Zenodo.
[9] A.C. Soares Sabioni, About the oxygen diffusion mechanism in ZnO, Solid State Ion. 170 (1) (2004) 145–148.
[10] A.C.S. Sabioni, M.J.F. Ramos, W.B. Ferraz, Oxygen diffusion in pure and doped ZnO, Mater. Res. 6 (2) (2003) 173–178.
[11] P. Erhart, K. Albe, Diffusion of zinc vacancies and interstitials in zinc oxide, Appl. Phys. Lett. 88 (20) (2006), 201918.
[12] N.S. Parmar, L.A. Boatner, K.G. Lynn, J.W. Choi, Zn vacancy formation energy and diffusion coefficient of CVT ZnO crystals in the sub-surface micron region, Sci. Rep. 8 (1) (2018) 13446.
[13] V. Yurkiv, T. Foroozan, A. Ramasubramanian, M. Ragone, S. Sharifi-Asl, R. Paoli, R. Shahbazian-Yassar, F. Mashayek, The mechanism of Zn diffusion through ZnO in secondary battery: a combined theoretical and experimental study, J. Phys. Chem. C 124 (29) (2020) 15730–15738.
[14] W.J. Moore, J.K. Lee, Kinetics of the formation of oxide films on zinc foil, Trans. Faraday Soc. 47 (0) (1951) 501–508.
[15] H. Delalu, J.R. Vignalou, M. Elkhatib, R. Metz, Kinetics and modeling of diffusion phenomena occurring during the complete oxidation of zinc powder: influence of granulometry, temperature and relative humidity of the oxidizing fluid, Solid State Sci. 2 (2) (2000) 229–235.
[16] C.D.S. Tuck, M.E. Whitehead, R.E. Smallman, A fundamental study of the kinetics of zinc oxidation in the temperature range 320–415°C in atmospheres of pure oxygen and oxygen doped with gaseous impurities, Corros. Sci. 21 (5) (1981) 333–352.
[17] J. Jedlinski, G. Borchardt, On the oxidation mechanism of alumina formers, Oxid. Met. 36 (3) (1991) 317–337.
[18] B.A. Pint, J.R. Martin, L.W. Hobbs, 18O/SIMS characterization of the growth mechanism of doped and undoped α-Al2O3, Oxid. Met. 39 (3) (1993) 167–195.